

Dependence of atmospheric muon rate on seawater depth measured with the first KM3NeT detection units

The KM3NeT Collaboration

M. Ageron¹, S. Aiello², F. Ameli³, M. Andre⁴, G. Androulakis⁵,
M. Anghinolfi⁶, G. Anton⁷, M. Ardid⁸, J. Aublin⁹, C. Bagatelas⁵,
G. Barbarino^{10,11}, B. Baret⁹, S. Basegmez du Pree¹²,
A. Belias⁵, E. Berbee¹², A. M. van den Berg¹³, V. Bertin¹,
V. van Beveren¹², S. Biagi^{14,a}, A. Biagioni³, S. Bianucci¹⁵,
M. Billault¹, M. Bissinger⁷, R. de Boer¹², J. Boumaaza¹⁶,
S. Bourret⁹, M. Bouta¹⁷, M. Bouwhuis¹², C. Bozza¹⁸, H. Brânzaș¹⁹,
M. Briel^{12,20}, M. Bruchner⁷, R. Bruijn^{12,20}, J. Brunner¹, E. Buis²¹,
R. Buompane^{10,22}, J. Busto¹, G. Cacopardo¹⁴, L. Caillat¹,
C. Cali¹⁴, D. Calvo²³, A. Capone^{24,3}, S. Celli^{24,3,50}, M. Chabab²⁵,
N. Chau⁹, S. Cherubini^{14,26}, V. Chiarella²⁷, T. Chiarusi²⁸,
M. Circella²⁹, R. Cocimano¹⁴, J. A. B. Coelho⁹, A. Coleiro²³,
M. Colomer Molla^{9,23}, S. Colonges⁹, R. Coniglione¹⁴, A. Cosquer¹,
P. Coyle¹, A. Creusot⁹, G. Cuttone¹⁴, C. D'Amato¹⁴, A. D'Amico¹²,
A. D'Onofrio^{10,22}, R. Dallier³⁰, M. De Palma^{29,31}, C. De Sio¹⁸,
I. Di Palma^{24,3}, A. F. Díaz³², D. Diego-Tortosa⁸, C. Distefano¹⁴,
A. Domi^{6,1,33}, R. Donà^{28,34}, C. Donzaud⁹, L. van Dooren²¹,
D. Dornic¹, M. Dörr³⁵, M. Durocher^{14,50}, T. Eberl⁷, T. van Eeden¹²,
I. El Bojaddaini¹⁷, H. Eljarrari¹⁶, D. Elsaesser³⁵, A. Enzenhöfer¹,
P. Fermani^{24,3}, G. Ferrara^{14,26}, M. D. Filipović³⁶, L. A. Fusco⁹,
D. Gajanana¹², T. Gal⁷, A. Garcia Soto¹², F. Garufi^{10,11},
L. Gialanella^{10,22}, E. Giorgio¹⁴, A. Giuliani³⁷, S. R. Gozzini²³,
R. Gracia³⁸, K. Graf⁷, D. Grasso¹⁵, T. Grégoire⁹, G. Grella¹⁸,
A. Grimaldi², A. Grmek¹⁴, D. Guderian⁵¹, M. Guerzoni²⁸,
C. Guidi^{6,33}, S. Hallmann⁷, H. Hamdaoui¹⁶, H. van Haren³⁹,
A. Heijboer¹², A. Hekalo³⁵, S. Henry¹, J. J. Hernández-Rey²³,
J. Hofestädt⁷, F. Huang³⁸, E. Huesca Santiago¹², G. Illuminati²³,
C. W. James⁴⁰, P. Jansweijer¹², M. Jongen¹², M. de Jong¹²,
P. de Jong^{12,20}, M. Kadler³⁵, P. Kalaczyński⁴¹, O. Kalekin⁷,
U. F. Katz⁷, F. Kayzel¹², P. Keller¹, N. R. Khan Chowdhury²³,
F. van der Knaap²¹, E. N. Koffeman^{12,20}, P. Kooijman^{20,52},
J. Koopstra¹², A. Kouchner^{9,42}, M. Kreter³⁵, V. Kulikovskiy⁶,
Meghna K. K.⁴¹, R. Lahmann⁷, P. Lamare¹, G. Larosa¹⁴,
J. Laurence¹, R. Le Breton⁹, F. Leone^{14,26}, E. Leonora²,
G. Levi^{28,34}, F. Librizzi², M. Lincetto^{1,b}, P. Litrico¹⁴,
C. D. Llorens Alvarez⁸, A. Lonardo³, F. Longhitano²,
D. Lopez-Coto⁴³, G. Maggi¹, J. Mańczak²³, K. Mannheim³⁵,
A. Margiotta^{28,34}, A. Marinelli^{44,15}, C. Markou⁵, L. Martin³⁰,
J. A. Martínez-Mora⁸, A. Martini²⁷, F. Marzaioli^{10,22},
R. Mele^{10,11}, K. W. Melis^{12,c}, P. Migliozi¹⁰, E. Migneco¹⁴,
P. Mijakowski⁴¹, L. S. Miranda⁴⁵, C. M. Mollo¹⁰, M. Mongelli²⁹,
M. Morganti^{15,53}, M. Moser⁷, A. Moussa¹⁷, R. Muller¹²,
P. Musico⁶, M. Musumeci¹⁴, L. Nauta¹², S. Navas⁴³, C. A. Nicolau³,
C. Nielsen⁹, B. Ó Fearraigh¹², M. Organokov³⁸, A. Orlando¹⁴,
V. Panagopoulos⁵, G. Pancaldi²⁸, G. Papalashvili⁴⁶, R. Papaleo¹⁴,
C. Pastore²⁹, G. E. Pávālas¹⁹, G. Pellegrini²⁸, C. Pellegrino^{34,54},

M. Perrin-Terrin¹, P. Piattelli¹⁴, K. Pikounis⁵, O. Pisanti^{10,11},
C. Poirè⁸, G. Polydefki⁵, V. Popa¹⁹, M. Post²⁰, T. Pradier³⁸,
G. Pühlhofer⁴⁷, S. Pulvirenti¹⁴, L. Quinn¹, F. Raffaelli¹⁵,
N. Randazzo², A. Rapicavoli²⁶, S. Razzaque⁴⁵, D. Real²³,
S. Reck⁷, J. Reubelt⁷, G. Riccobene¹⁴, L. Rigalleau³⁰, G. Rizza²,
R. Rocco¹⁰, A. Rovelli¹⁴, J. Royon¹, M. Salemi², I. Salvadori¹,
D. F. E. Samtleben^{12,48}, A. Sánchez Losa²⁹, M. Sanguineti^{6,33},
A. Santangelo⁴⁷, D. Santonocito¹⁴, P. Sapienza¹⁴, J. Schmelling¹²,
V. Sciacca¹⁴, D. Sciliberto², J. Seneca¹², I. Sgura²⁹, R. Shanidze⁴⁶,
A. Sharma⁴⁴, F. Simeone³, A. Sinopoulou⁵, B. Spisso^{18,10},
M. Spurio^{28,34}, D. Stavropoulos⁵, J. Steijger¹², S. M. Stellacci^{18,10},
B. Strandberg¹², D. Stransky⁷, T. Stüven⁷, M. Taiuti^{6,33},
Y. Tayalati¹⁶, E. Tenllado⁴³, D. Tézier¹, T. Thakore²³,
S. Theraube¹, P. Timmer¹², S. Tingay⁴⁰, A. Trovato¹⁴,
S. Tsagkli⁵, E. Tzamariudaki⁵, D. Tzanetatos⁵, C. Valieri²⁸,
V. Van Elewyck^{9,42}, F. Versari^{28,34}, S. Viola¹⁴, D. Vivolo^{10,11},
G. de Wasseige⁹, J. Wilms⁴⁹, R. Wojaczyński⁴¹, E. de Wolf^{12,20},
D. Zaborov¹, A. Zegarelli^{24,3}, J. D. Zornoza²³, J. Zúñiga²²

- ¹ Aix Marseille Univ, CNRS/IN2P3, CPPM, Marseille, France
- ² INFN, Sezione di Catania, Via Santa Sofia 64, Catania, 95123 Italy
- ³ INFN, Sezione di Roma, Piazzale Aldo Moro 2, Roma, 00185 Italy
- ⁴ Universitat Politècnica de Catalunya, Laboratori d'Aplicacions Bioacústiques, Centre Tecnològic de Vilanova i la Geltrú, Avda. Rambla Exposició, s/n, Vilanova i la Geltrú, 08800 Spain
- ⁵ NCSR Demokritos, Institute of Nuclear and Particle Physics, Ag. Paraskevi Attikis, Athens, 15310 Greece
- ⁶ INFN, Sezione di Genova, Via Dodecaneso 33, Genova, 16146 Italy
- ⁷ Friedrich-Alexander-Universität Erlangen-Nürnberg, Erlangen Centre for Astroparticle Physics, Erwin-Rommel-Straße 1, 91058 Erlangen, Germany
- ⁸ Universitat Politècnica de València, Instituto de Investigación para la Gestión Integrada de las Zonas Costeras, C/ Paranimf, 1, Gandia, 46730 Spain
- ⁹ APC, Université Paris Diderot, CNRS/IN2P3, CEA/IRFU, Observatoire de Paris, Sorbonne Paris Cité, 75205 Paris, France
- ¹⁰ INFN, Laboratori Nazionali del Sud, Via S. Sofia 62, Catania, 95123 Italy
- ¹¹ Università di Napoli "Federico II", Dip. Scienze Fisiche "E. Pancini", Complesso Universitario di Monte S. Angelo, Via Cintia ed. G, Napoli, 80126 Italy
- ¹² Nikhef, National Institute for Subatomic Physics, PO Box 41882, Amsterdam, 1009 DB Netherlands
- ¹³ KVI-CART University of Groningen, Groningen, the Netherlands
- ¹⁴ INFN, Laboratori Nazionali del Sud, Via S. Sofia 62, Catania, 95123 Italy
- ¹⁵ INFN, Sezione di Pisa, Largo Bruno Pontecorvo 3, Pisa, 56127 Italy
- ¹⁶ University Mohammed V in Rabat, Faculty of Sciences, 4 av. Ibn Battouta, B.P. 1014, R.P. 10000 Rabat, Morocco
- ¹⁷ University Mohammed I, Faculty of Sciences, BV Mohammed VI, B.P. 717, R.P. 60000 Oujda, Morocco
- ¹⁸ Università di Salerno e INFN Gruppo Collegato di Salerno, Dipartimento di Fisica, Via Giovanni Paolo II 132, Fisciano, 84084 Italy
- ¹⁹ ISS, Atomistilor 409, Măgurele, RO-077125 Romania
- ²⁰ University of Amsterdam, Institute of Physics/IHEF, PO Box 94216, Amsterdam, 1090 GE Netherlands
- ²¹ TNO, Technical Sciences, PO Box 155, Delft, 2600 AD Netherlands
- ²² Università degli Studi della Campania "Luigi Vanvitelli", Dipartimento di Matematica e Fisica, viale Lincoln 5, Caserta, 81100 Italy
- ²³ IFIC - Instituto de Física Corpuscular (CSIC - Universitat de València), c/Catedrático José Beltrán, 2, 46980 Paterna, Valencia, Spain
- ²⁴ Università La Sapienza, Dipartimento di Fisica, Piazzale Aldo Moro 2, Roma, 00185 Italy
- ²⁵ Cadi Ayyad University, Physics Department, Faculty of Science Semlalia, Av. My Abdellah, P.O.B. 2390, Marrakech, 40000 Morocco
- ²⁶ Università di Catania, Dipartimento di Fisica e Astronomia, Via Santa Sofia 64, Catania, 95123 Italy
- ²⁷ INFN, LNF, Via Enrico Fermi, 40, Frascati, 00044 Italy
- ²⁸ INFN, Sezione di Bologna, v.le C. Berti-Pichat, 6/2, Bologna, 40127 Italy
- ²⁹ INFN, Sezione di Bari, Via Amendola 173, Bari, 70126 Italy
- ³⁰ Subatech, IMT Atlantique, IN2P3-CNRS, 4 rue Alfred Kastler - La Chantrerie, Nantes, BP 20722 44307 France
- ³¹ University of Bari, Via Amendola 173, Bari, 70126 Italy
- ³² University of Granada, Dept. of Computer Architecture and Technology/CITIC, 18071 Granada, Spain
- ³³ Università di Genova, Via Dodecaneso 33, Genova, 16146 Italy
- ³⁴ Università di Bologna, Dipartimento di Fisica e Astronomia, v.le C. Berti-Pichat, 6/2, Bologna, 40127 Italy
- ³⁵ University Würzburg, Emil-Fischer-Straße 31, Würzburg, 97074 Germany
- ³⁶ Western Sydney University, School of Computing, Engineering and Mathematics, Locked Bag 1797, Penrith, NSW 2751 Australia
- ³⁷ Università di Pisa, DIMNP, Via Diotallevi 2, Pisa, 56122 Italy
- ³⁸ Université de Strasbourg, CNRS, IPHC, 23 rue du Loess, Strasbourg, 67037 France
- ³⁹ NIOZ (Royal Netherlands Institute for Sea Research) and Utrecht University, PO Box 59, Den Burg, Texel, 1790 AB, the Netherlands
- ⁴⁰ Curtin University, Curtin Institute of Radio Astronomy, GPO Box U1987, Perth, WA 6845 Australia
- ⁴¹ National Centre for Nuclear Research, 00-681 Warsaw, Poland
- ⁴² Institut Universitaire de France, 1 rue Descartes, Paris, 75005 France
- ⁴³ University of Granada, Dpto. de Física Teórica y del Cosmos & C.A.F.P.E., 18071 Granada, Spain
- ⁴⁴ Università di Pisa, Dipartimento di Fisica, Largo Bruno Pontecorvo 3, Pisa, 56127 Italy
- ⁴⁵ University of Johannesburg, Department Physics, PO Box 524, Auckland Park, 2006 South Africa
- ⁴⁶ Tbilisi State University, Department of Physics, 3, Chavchavadze Ave., Tbilisi, 0179 Georgia
- ⁴⁷ Eberhard Karls Universität Tübingen, Institut für Astronomie und Astrophysik, Sand 1, Tübingen, 72076 Germany
- ⁴⁸ Leiden University, Leiden Institute of Physics, PO Box 9504, Leiden, 2300 RA Netherlands
- ⁴⁹ Friedrich-Alexander-Universität Erlangen-Nürnberg, Remeis Sternwarte, Sternwartstraße 7, 96049 Bamberg, Germany
- ⁵⁰ Gran Sasso Science Institute, GSSI, Viale Francesco Crispi 7, L'Aquila, 67100 Italy
- ⁵¹ University of Münster, Institut für Kernphysik, Wilhelm-Klemm-Str. 9, Münster, 48149 Germany
- ⁵² Utrecht University, Department of Physics and Astronomy, PO Box 80000, Utrecht, 3508 TA Netherlands
- ⁵³ Accademia Navale di Livorno, Viale Italia 72, Livorno, 57100 Italy
- ⁵⁴ INFN, CNAF, v.le C. Berti-Pichat, 6/2, Bologna, 40127 Italy

Received: / Accepted:

^aCorresponding author: simone.biagi@infn.it

^bCorresponding author: lincetto@cppm.in2p3.fr

^cCorresponding author: kmelis@nikhef.nl

Abstract KM3NeT is a research infrastructure located in the Mediterranean Sea, that will consist of two deep-sea Cherenkov neutrino detectors. With one detector (ARCA), the KM3NeT Collaboration aims at identifying and studying TeV-PeV astrophysical neutrino sources. With the other detector (ORCA), the neutrino mass ordering will be determined by studying GeV-scale atmospheric neutrino oscillations. The first KM3NeT detection units were deployed at the Italian and French sites between 2015 and 2017. In this paper, a description of the detector is presented, together with a summary of the procedures used to calibrate the detector in-situ. Finally, the dependence of muon rate between 2232–3386 m seawater depth is compared with a parameterisation of the underwater muon flux.

1 Introduction

The KM3NeT (km³-scale neutrino telescope) Collaboration is establishing a research facility in the Mediterranean Sea that will host a network of neutrino detectors [1]. Neutrinos represent an alternative to photons and cosmic rays to explore the high-energy Universe. They can emerge from dense objects and travel large distances, without being deflected by magnetic fields or interacting with radiation and matter. In addition, the neutrino mass ordering can be determined using neutrinos produced in the earth atmosphere through interactions of cosmic rays [1].

The ARCA (Astroparticle Research with Cosmics in the Abyss) detector is being installed at the KM3NeT-It site, 80 km offshore the Sicilian coast in front of Capo Passero (Italy) at a sea bottom depth of about 3450 m. The main physics goal of ARCA is the discovery and subsequent observation of astrophysical neutrino sources in the Universe [2]. About 1 km³ of seawater will be instrumented with $\sim 130,000$ photomultiplier tubes (PMTs) for the detection of Cherenkov light induced by charged particles produced in neutrino interactions. The geometry of ARCA is optimised to maximise its detection efficiency in the neutrino energy range 1 TeV–10 PeV.

In parallel, the KM3NeT Collaboration started the construction of the ORCA (Oscillation Research with Cosmics in the Abyss) detector at the KM3NeT-Fr site, 40 km offshore Toulon (France) at a sea bottom depth of about 2450 m. ORCA shares the same technology and detector elements as ARCA, but in a denser configuration to detect neutrinos in the range 1–100 GeV. ORCA instruments a volume of about 8 Mton. The main physics goal is the determination of the neutrino mass ordering by measuring the oscillation probabilities of atmospheric neutrinos [1, 3].

In this paper, a procedure to calibrate the PMT detection efficiencies using the light emitted by ⁴⁰K decays is discussed. The flux of atmospheric muons produced in cosmic ray air showers forms a background to the primary objective of KM3NeT. A measurement of the depth dependence of the atmospheric muon flux will be presented. This measurement is used to verify the calibration procedure. The results are obtained with the first two detection units of ARCA (detector configuration referred to as ARCA2) and the first one of ORCA (ORCA1).

In Section 2, an overview of the ARCA and ORCA detectors and their detection elements is given. Section 3 outlines the time and photon detection efficiency calibration procedures. Section 4 presents the data samples used in the analysis. The algorithms used to simulate the detector behaviour are described in Section 5. An indirect measurement of the atmospheric muon flux depth dependence is reported and discussed in Section 6. Finally, the conclusions are given in Section 7.

2 The KM3NeT detectors

ARCA and ORCA consist of three dimensional arrays of Digital Optical Modules (DOMs), installed in the deep waters of the Mediterranean Sea. The DOM is a pressure-resistant glass sphere housing 31 PMTs of 80 mm diameter each (see Figure 1). These PMTs detect the Cherenkov light induced by relativistic charged particles propagating through the seawater. A transparent gel is employed to guarantee the optical coupling between the PMTs and the internal surface of the glass spheres. A reflector ring is mounted around each PMT to enhance its sensitive area [4].

Several instruments are mounted inside the DOM to measure its position and orientation (compass, tilt-meter, acoustic sensor) and to time-calibrate the DOMs (light emitters based on LEDs). The real-time positioning of the DOMs is necessary as the detector elements can move under the influence of sea currents. A description of the DOM is given in Refs. [5, 6].

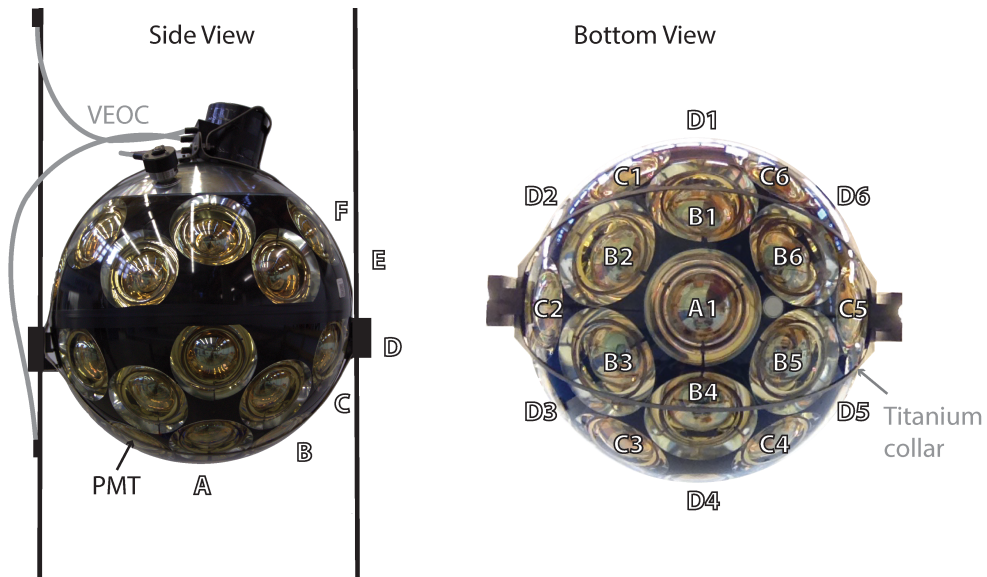


Fig. 1 Side view (left) and bottom view (right) of a KM3NeT DOM. See text for explanation of highlighted (mechanical) parts. The naming convention of the PMTs in rings and numbers is indicated.

A KM3NeT detection unit (DU) is a series of 18 DOMs connected by an electro-optical cable and arranged in a flexible and slender vertical string. The glass sphere of each DOM is encircled by a titanium collar which is attached to two 4 mm diameter ropes (Figure 1). Each DU is anchored to the seabed using a dead weight. A buoy is connected at the top of the DU to keep it close to vertical.

A set of 115 detection units constitutes a building block of the KM3NeT detectors. ARCA and ORCA differ in the granularity of the sensor modules. For the ARCA-type detection unit the vertical distance between the DOMs is 36 m, resulting in a total height of the structure of 700 m. The installation of two ARCA building blocks at the KM3NeT-It site is planned, with a horizontal distance between the DUs of about 90 m and a total instrumented volume of about 1 km³. In the detection units of ORCA, the DOMs are mounted at an average vertical distance of about 9 m from each other, and the total height of the unit is 250 m. ORCA plans the construction of one building block with a distance between the detection units of about 20 m.

The analog signals from the PMTs are digitised using a custom electronic board mounted inside each DOM [7]. When one or more photons impinge on the PMT photocathode and the anode electrical signal crosses the threshold of a discriminator, a level zero (L0) hit is recorded. The crossing time and the time-over-threshold (ToT) of the waveform are recorded. The ToT gives a measure of the pulse amplitude. The high voltage setting of each PMT is tuned in-situ to give an average ToT of 26.4 ns for a single photoelectron (p.e.). A default value corresponding to 0.3 p.e. is set for the discriminator threshold.

With an *all-data-to-shore* approach [8], no data reduction is applied underwater. All L0 hits are assembled in time windows with a fixed size of 100 ms, called *L0 timeslices*. The timeslices are sent to a computer farm at the shore station via a network of submarine cables and junction boxes.

The DU base contains the power and control electronics and the components of the optical network for the communication between the DOMs and the onshore station. It consists of a titanium cylinder attached to the anchor. For power delivery and data transmission, a Vertical Electro-Optical Cable (VEOC) is attached to each DOM. The VEOC is a pressure-balanced, oil-filled, plastic tube that contains two copper wires for the power delivery (400 V DC) and 18 optical fibres for the data transmission. Two power conductors and a single fibre are branched out at the level of each DOM via a so-called breakout box. The breakout box contains a DC/DC converter (400 V to 12 V) to supply each DOM with a suitable voltage. The power conductors and optical fibre enter the glass sphere through a pressure-resistant penetrator.

Onshore, once the time calibration is applied, dedicated trigger algorithms look in parallel for the physics events to be saved for offline analysis. A detailed discussion of trigger algorithms is reported in Ref. [1]. A level one (L1) coincidence is composed of two or more L0 hits on the same DOM within a time window of 25 ns.

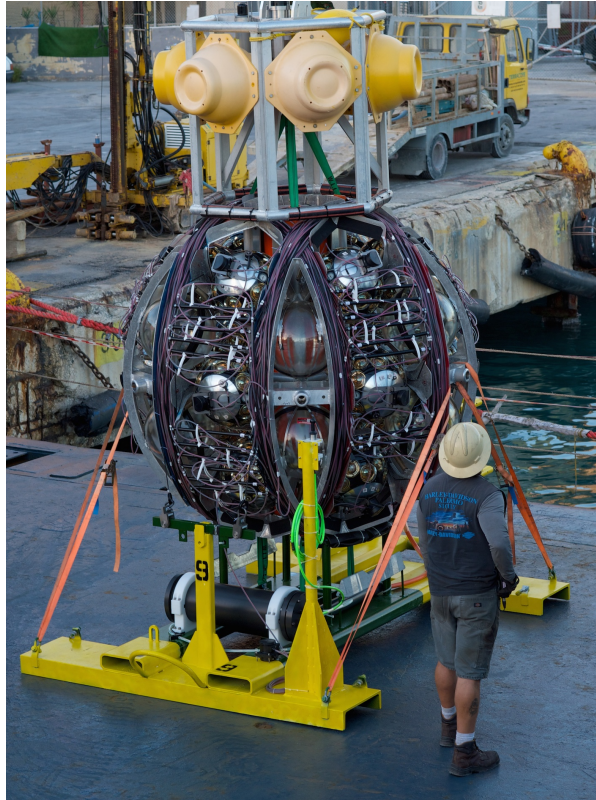


Fig. 2 A detection unit arranged on the launcher vehicle, ready to be deployed during a sea campaign. The yellow buoyancy system is visible on top of it.

Timeslices of L1 coincidences are stored for calibration and monitoring. In this paper, the L1 timeslices data are used.

The data acquisition system must be able to handle the large data throughput produced by the detector [9]. The average observed hit rate, dominated by the decay of ^{40}K isotopes in the seawater, is about 7 kHz per PMT, corresponding to about 13 Mbps of data per DOM. Occasionally, the rate can be higher due to bioluminescence activity. Bioluminescence is characterised by an increase (up to the MHz range) of the hit rate, lasting up to several seconds. The readout system of the DOM disables the channel acquisition as soon as the rate is estimated to be over 20 kHz (*high rate veto*).

For the deployment, the DU is furled onto a spherical structure with a radius of approximately 2 m, called the Launcher of Optical Modules (LOM) [10], as can be seen in Figure 2. Once at the seabed, the DU is connected to the seafloor network using a Remotely Operated Vehicle (ROV). After confirming the functionality of the DOMs, the LOM is remotely released and floats up to the surface, progressively unfurling the detection unit.

The first DU of the ARCA detector was deployed in December 2015, followed by two DUs in May 2016. The vertical alignment of the DUs was confirmed by visual inspection using the ROV. Data taking started immediately after deployment. One of the units deployed in May 2016 was recovered for inspection in July 2016. Due to electrical problems in the network infrastructure at the seabed, the operations at the KM3NeT-It site were on hold between April 2017 and January 2019, after which data taking continued. The DU of ORCA1 was installed in September 2017 and operated until mid-December 2017, when a failure of the main electro-optical cable occurred. The data taking was resumed in February 2019 following the replacement of a part in the main cable.

3 Time and efficiency calibration

The majority of light observed by the PMTs originates from the decays of the radioactive ^{40}K isotope naturally abundant in sea salt. The Cherenkov light produced by the secondary electrons of the decay represents the main

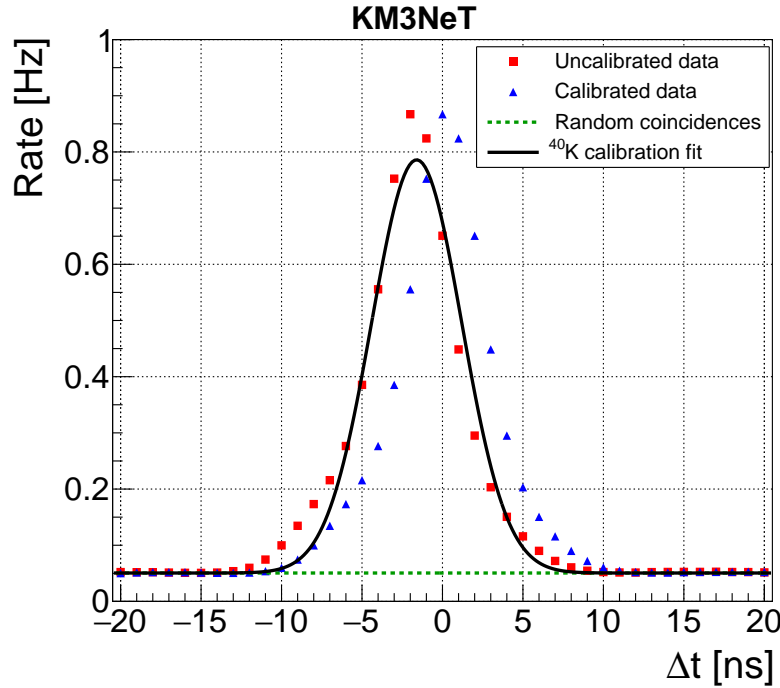


Fig. 3 Distribution of time differences between hits in coincidence for one typical pair of adjacent PMTs, before (red) and after (blue) calibration. In these, only statistical errors are shown, which are smaller than the symbols. A peak due to genuine ^{40}K coincidences is observed above a flat background (green). The black line is a Gaussian fit of the calibration model (see text) to the uncalibrated data of all PMT pairs.

optical background for deep-sea neutrino detectors, but it is removed by requiring space-time correlations between DOMs. On the other hand, the ^{40}K signature is particularly useful for in-situ calibration of the PMTs contained in a single DOM (intra-DOM calibration) and for long-term monitoring of the performance of the detector.

The distribution of the time differences of L0 hits seen in coincidence by two PMTs i, j is used to determine the relative time offset (t_0), the transit time spread (TTS) and the photon detection efficiency (ϵ) of the two PMTs involved [11]. Here the time offset of each PMT in a DOM compensates for the (mean) transit time and differences in propagation time of the electrical signal of each PMT. Only the differences between the time offsets of the PMTs within a DOM can be fitted using this procedure. The average time offset of the PMTs in a DOM is set to zero. The PMT photon detection efficiency reflects the combined effect of the PMT quantum efficiency, the collection efficiency, the angular acceptance of the PMT and absorption in the gel and the glass. In a DOM with $N = 31$ PMTs, all the unique PMT pairs are taken into account, which corresponds to $N(N - 1)/2 = 465$ pairs. Random coincidences of uncorrelated hits give an offset of the observed coincidence rate, independent of the hit time difference. This contribution is estimated from the observed L0 rates, and checked to be compatible with a fit to the tails of the distribution. After subtracting the random coincidence rate, the 465 coincidence distributions of all PMT pairs within a DOM are simultaneously fitted with a Gaussian with mean $t_{0i} - t_{0j}$, variance $(TTS_i)^2 + (TTS_j)^2$ and area $f(\theta_{i,j}) \cdot \epsilon_i \cdot \epsilon_j$. The function $f(\theta_{i,j})$ is the expected coincidence rate as a function of the space angle $\theta_{i,j}$ between the two PMTs. This parameterisation follows from dedicated simulations using a nominal DOM model [12]. The function used is an updated version of the parameterisation presented in Ref. [11].

In Figure 3, the time difference distribution of one pair of PMTs (in this case two adjacent PMTs) is shown. The data before calibration (red) and after calibration (blue) are reported. The fitted random coincidence rate is shown in green. The result of the fit to all 465 PMT pairs is shown in black. The difference between the measured distribution and the Gaussian fit can be explained as the result of non-Gaussian transit time distribution of the PMTs. The calibrated hit time difference distribution, shifted according to the fitted time offsets from the procedure outlined above, is shown in blue. As expected, the mean of the calibrated time difference distribution is zero.

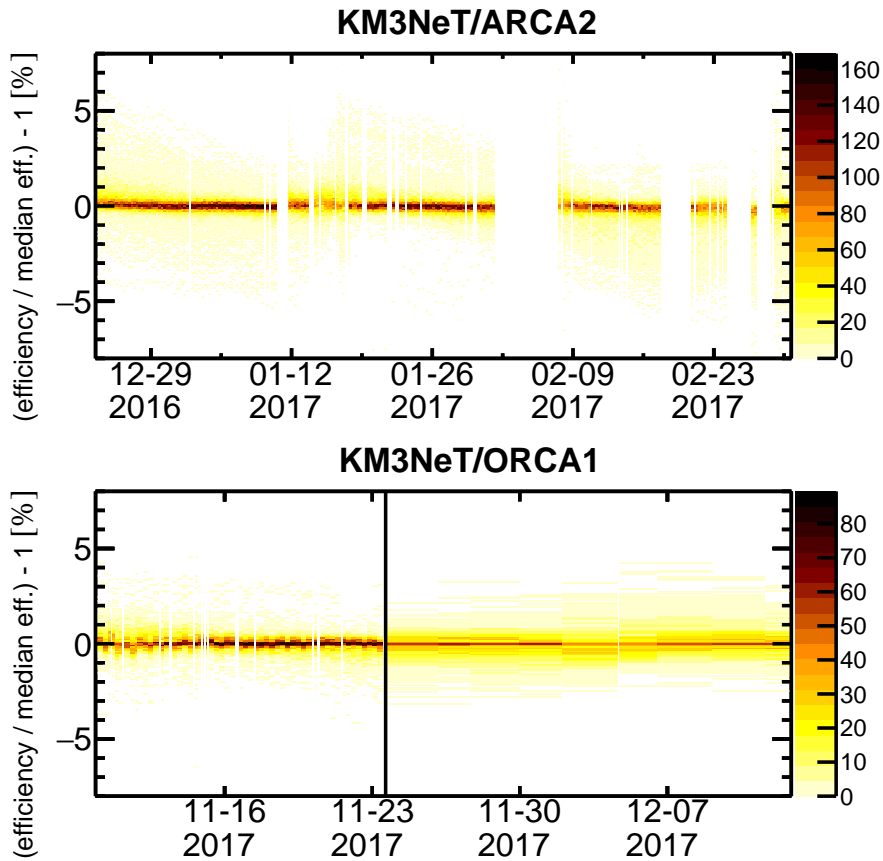


Fig. 4 Deviation of the estimated photon detection efficiency for each PMT with respect to its global median efficiency for the ARCA2 and ORCA1 detectors as a function of time. The color scale indicates the number of PMTs in each bin. Vertical white bands reflect the periods without data-taking; the vertical black line represents the time at which the L1 data stream downscaling was introduced (see text).

The obtained intra-DOM time offsets are used to calibrate data in the offline analysis, while the PMT efficiencies are used in simulations (see Section 5). The time calibration between DOMs (inter-DOM calibration) is done with calibrated laser pulses before DU deployment. In-situ, the inter-DOM time calibration is refined exploiting the signals from the LED beacons on each DOM and using atmospheric muons [11]. This paper does not cover the inter-DOM calibration as the reported results are obtained from standalone DOM data.

4 Data sample

The selected data taking period for the ARCA2 detector ranges from December 23, 2016 to March 2, 2017. At the beginning of February 2017, an interruption of the operation of ARCA2 of approximately one week happened due to an electrical problem in the onshore infrastructure. The selected data taking period for the ORCA1 detector is from November 9, 2017 to December 13, 2017. From November 23 2017, the timeslice data of ORCA 1 has been downsampled by a factor 20, in order to reduce the amount of data written on disk. In this analysis, the data from a DOM with one or more PMTs in high-rate-veto (see Section 2) are ignored on a timeslice basis.

The combined PMT time offset and PMT photon detection efficiency calibration has been performed over segments of 6 hours of data taking, which provide sufficient statistics to prevent fluctuations in the parameter estimations used for data analysis and simulation. In Figure 4, the stability of photon detection efficiencies is evaluated by plotting for each individual PMT the deviation of the efficiency with respect to its median efficiency estimated from the entire period of data taking. The efficiencies are stable in time, as the root mean square (RMS) of the distribution of the deviations is 0.5% for ORCA1 and 0.8% for ARCA2 in the considered data taking period. The fitted PMT photon detection efficiencies of the six lowest DOMs of ORCA1 are approximately 15%

lower than the average efficiency of the other ORCA and ARCA DOMs. A similar pattern is observed in the single hit rates of these PMTs. Investigations are in progress to understand the origin of this difference.

5 Monte Carlo simulations

The response of the detector has been studied in detail using Monte Carlo simulated atmospheric muon events. The Monte Carlo chain is based on a multi-stage approach comprising an event generator, a simulator of the Cherenkov light and a stage which covers the combination of the simulation of the PMT response, the readout and the onshore data filtering.

Atmospheric muon events have been generated using the MUPAGE package [13]. This software provides a parametric calculation of the underwater muon flux of atmospheric muon (bundles), based on a full Monte Carlo simulation of the primary cosmic ray interactions and shower propagation in the atmosphere. With MUPAGE, muon bundles have been generated with a bundle energy E_b above 10 GeV over the surface of a cylinder which extends the instrumented volume by 280 m. Light emitted by muons simulated outside of this volume have a negligible probability to produce at least one L1 coincidence.

The tracking of muons in seawater and subsequent production and propagation of the Cherenkov light are implemented in the KM3 [14] software package. KM3 uses tabulated results from a full GEANT3.21 [15] simulation of relativistic muons and electromagnetic showers. In this, the Cherenkov light production, propagation, scattering and absorption in seawater are taken into account. In addition, KM3 also accounts for the effects associated with the DOM structure, such as the reflector rings and the light absorption in the glass and optical gel.

Using custom KM3NeT software, the detector response is simulated. Random optical background hits are added according to single hit and coincidence rates observed in data. The PMT response is then simulated according to the measured transit time distribution [16] and PMT parameters (photon detection efficiency, gain and gain-spread). In this, the PMT photon detection efficiencies can either be set to the nominal value, or to the measured values using the calibration procedure described in Section 3. The software is designed to produce a data format identical to the one produced by the DAQ system. As a result, the same algorithms can be applied independently on data and simulations.

6 Depth dependence of atmospheric muon rate

6.1 Optical background discrimination

The multi-PMT design of the DOM provides information on the number of photons as well as their arrival times and directions. This information is used to discriminate between the signals from atmospheric muons, bioluminescence and ^{40}K backgrounds. The discriminating power is mainly achieved by exploiting coincidences between different PMTs in the same DOM. In this analysis, a coincidence is defined as a sequence of hits in a DOM within a time window of 15 ns. The number of hit PMTs in a coincidence is called *multiplicity*.

In Figure 5, the coincidence rates, averaged over the DOMs of the ARCA2 and ORCA1 detectors respectively, are shown as a function of the multiplicity. In this, only statistical uncertainties are indicated. The random combinatorial background has been subtracted and the times of the hits have been calibrated as described in Section 3.

The contribution from ^{40}K decays is relevant up to a multiplicity of seven [17]. Conductivity measurements indicate the salinity in seawater to be independent of depth and detector site [18, 19]. Due to the difference in the average efficiency between the optical modules of the two detectors (see Section 4), the ^{40}K coincidence rates observed in ORCA1 are approximately 15% lower than the rates observed in ARCA2.

Coincidences from atmospheric muons dominate at a multiplicity of eight and higher as muon (bundles) can potentially illuminate all the PMTs of a single DOM. The ratio between ARCA2 and ORCA1 at high multiplicities, dominated by atmospheric muons, shows a factor three difference attributed to the different average depths of the DOMs, which is around 2310 m for ORCA and 3070 m for ARCA. In Figure 6, the stability of the coincidences rates in the multiplicity region dominated by atmospheric muons is shown.

The relative contribution of PMTs to coincidences as a function of the multiplicity is shown in Figure 7. The lower DOM hemisphere is more populated at lower multiplicities due to the higher number of close-by

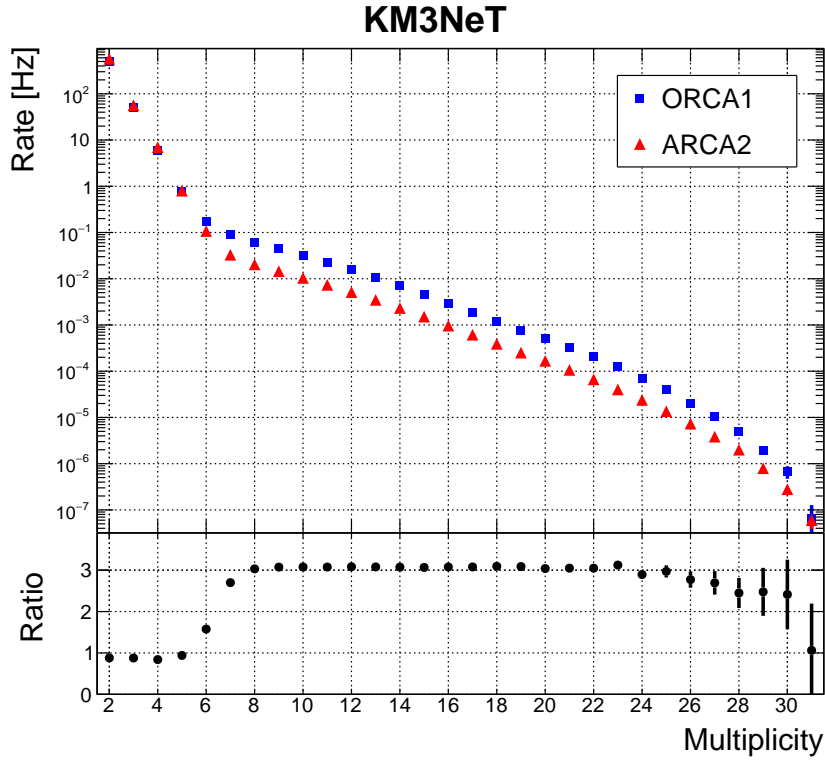


Fig. 5 Top: coincidence rates as a function of the multiplicity for the ORCA1 and ARCA2 detectors averaged over all the DOMs of each detector. Bottom: ratio between ORCA1 and ARCA2 coincidence rates. Up to a multiplicity of six, the coincidence rate is dominated by ^{40}K decays. Above a multiplicity of seven, atmospheric muons dominate. Only statistical errors are shown.

PMTs, resulting in more coincidences from ^{40}K decays. Shadowing effects of the rope-mounting structures can be observed for PMTs C2 and C5. On the other hand, the contribution to high multiplicities comes mostly from the upper hemisphere. This reflects the downgoing direction of atmospheric muons.

6.2 Muon-induced coincidence rates

As a result of energy losses in seawater, a lower rate of atmospheric muons is observed at larger depths. This is reflected in the average coincidence rates for multiplicities ≥ 8 between the two detectors (Figure 5). The ≥ 8 multiplicity coincidence rate for all the active DOMs of the two detectors is shown in Figure 8 as a function of the depth of each DOM.

Differences in the PMT photon detection efficiencies between the DOMs affect the measured rates, thereby affecting also the depth-dependence relation. In order to correct for this, two Monte Carlo simulations have been performed. In the first set of simulations, referred to as ‘uniform’, the photon detection efficiencies are set to the nominal value in order to establish the MC normalisation. In the second, the photon detection efficiencies are set to their measured values (see Section 3). The result is referred to as ‘calibrated’.

The ratio between the simulated rates is used to correct the measured rates for each DOM, $R_{\text{measured}}^{\text{data}}$, applying the formula:

$$R_{\text{corrected}}^{\text{data}} = R_{\text{measured}}^{\text{data}} \cdot \frac{R_{\text{uniform}}^{\text{MC}}}{R_{\text{calibrated}}^{\text{MC}}}. \quad (1)$$

In Figure 8, the efficiency-corrected coincidence rates are shown in red. For the lowest six DOMs of ORCA1, the correction factor is larger than for ARCA2. This can be explained by the lower efficiencies of the PMTs of ORCA1 (see Section 4).

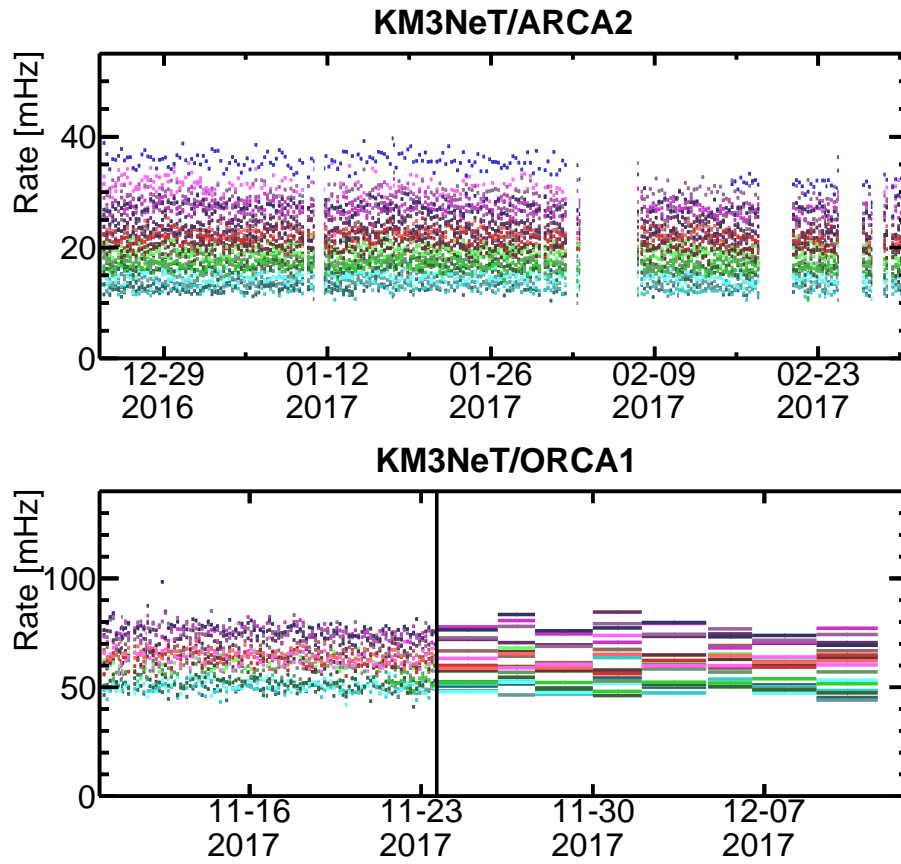


Fig. 6 Rate of multiplicity ≥ 8 coincidences as a function of time for the DOMs of the ARCA2 and ORCA1 detectors. Each point corresponds to one run and every colour to a single DOM. Vertical white bands are periods without data-taking. The vertical black line in the bottom plot represents the date at which the L1 data stream is downscaled (see Section 4).

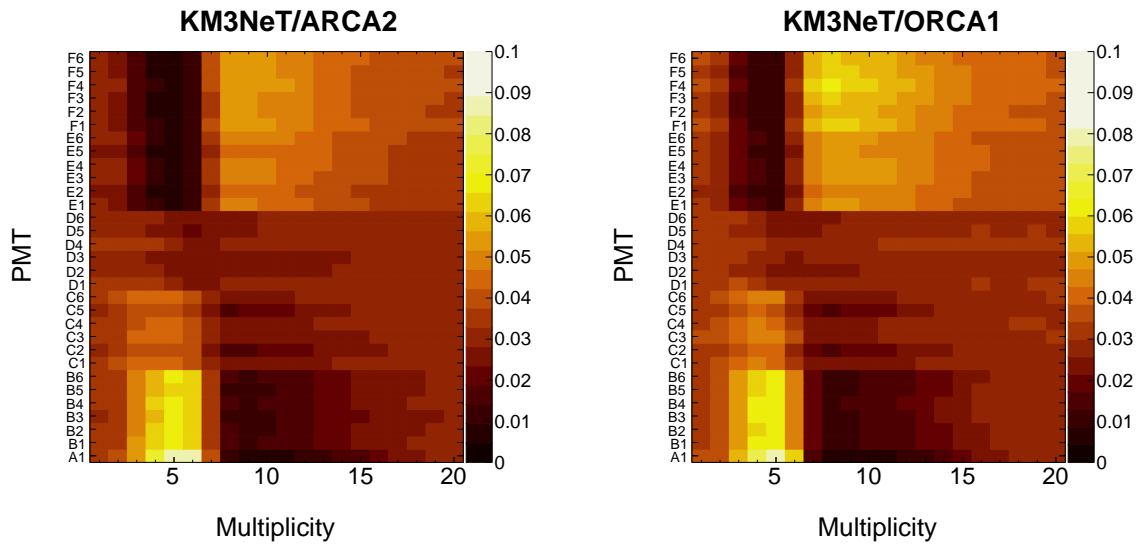


Fig. 7 Probability density function of the PMT contribution to coincidence rates as a function of the multiplicity (each abscissa bin is normalised to unity). The PMT is identified by the ring (letter) and the position of the PMT on the ring (number). The first address (A1) refers to the vertical down-facing PMT, rings from B to D belong to the lower hemisphere, while rings E and F belong to the upper hemisphere of the DOM (see Figure 1). Above a multiplicity of 20, statistical fluctuations dominate the pattern, and are therefore left out of the figure.

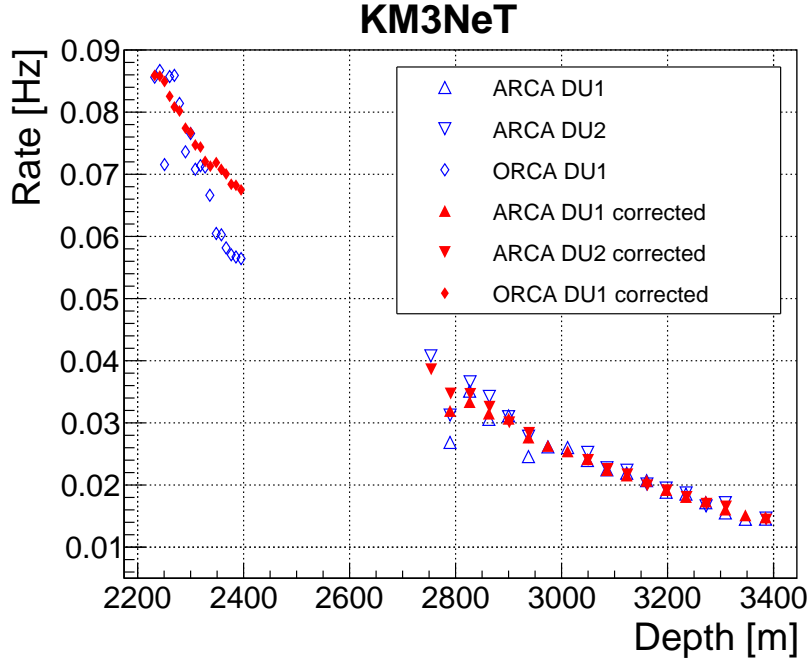


Fig. 8 Multiplicity ≥ 8 coincidence rate of all DOMs as function of depth below the sea level. The coincidence rates for the ARCA2 and ORCA1 detectors are reported as measured (blue points) and after the correction for the PMT photon detection efficiencies (red points). Statistical uncertainties are included and smaller than markers.

6.3 Comparison with a flux model

The depth dependence of the efficiency-corrected rates is compared with a model of the muon flux in Figure 9. For ARCA2, the rates of the DOMs at the same depth are averaged to get a single value.

The considered model from Bugaev et al. [20] provides an estimation of the underwater vertical atmospheric muon flux. The angle-integrated flux as a function of depth has been calculated from the formulas provided in Ref. [21]. In order to compare with the data, the atmospheric muon flux is described with a simple analytic expression in the form of a vertical flux $I_\mu(d, \theta = 0)$ corrected with a factor $C(d)$ that accounts for the angular integration. In the depth range of interest, the resulting expression reads as follows (where the water equivalent depth d accounts for the density of seawater):

$$I_\mu(d) = \frac{I_\mu(d, \theta = 0)}{C(d)} = \frac{A_1 \cdot e^{A_2 \cdot d} + A_3 \cdot e^{A_4 \cdot d}}{B_1 + B_2 \cdot d}, \quad (2)$$

$$\begin{aligned} A_1 &= 1.31 \times 10^{-5} \text{ cm}^{-2} \text{ s}^{-1} \text{ sr}^{-1}, \quad A_2 = -2.91 \times 10^{-3} \text{ m}^{-1}, \\ A_3 &= 7.31 \times 10^{-7} \text{ cm}^{-2} \text{ s}^{-1} \text{ sr}^{-1}, \quad A_4 = -1.17 \times 10^{-3} \text{ m}^{-1}, \\ B_1 &= 4.16 \times 10^{-1} \text{ sr}^{-1}, \quad B_2 = 1.07 \times 10^{-4} \text{ m}^{-1} \text{ sr}^{-1}. \end{aligned}$$

In this, the A_i parameters define the depth dependence of the vertical flux and the B_j parameters the integration factor. The reported parameters are valid for a flux of muons with energies above 1 GeV. Assuming a direct proportionality between the muon flux and the coincidence rate, the parametrisation has been fitted to the corrected rates using the function:

$$R(d) = R_0 \cdot I_\mu(d) \quad (3)$$

where $R(d)$ is the efficiency-corrected rate of multiplicities ≥ 8 as a function of depth. R_0 is a global normalisation factor and is the only free parameter of the fit. The depth dependence relation is in good agreement with the model of the muon flux, over a wide range of depths. The RMS of the residuals of the corrected data points compared to the fitted model is below 2%, underlining the reliability of the calibration procedure.

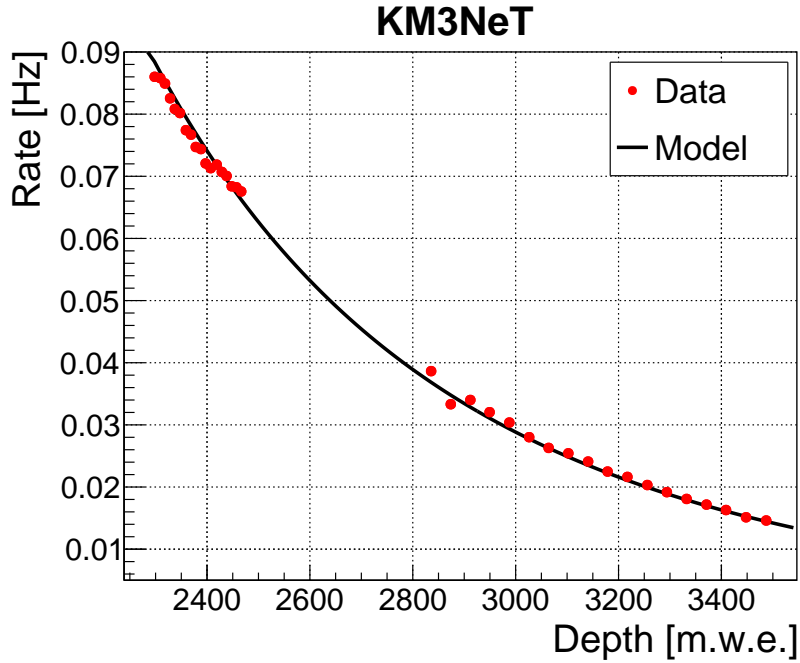


Fig. 9 Efficiency-corrected ≥ 8 multiplicity coincidence rates measured with the ORCA1 and ARCA2 detectors as a function of depth below the sea level (red points), fitted with the Bugaev model of the atmospheric muon flux (continuous black line). The depth is expressed in water equivalent (w.e.). Statistical uncertainties are included and smaller than markers.

6.4 Evaluation of systematic uncertainties

Applying a coincidence selection at a multiplicity higher than eight to estimate the muon-induced coincidence rates, the residuals of the fit maintain an RMS below 3%. This indicates that there are no significant systematic deviations in the choice of the multiplicity selection.

Using the nominal simulations, the ≥ 8 multiplicity coincidence rate of each DOM is compared to the simulated atmospheric muon flux at the corresponding depth. The value of R_0 is independent of depth within 4% over the considered depth interval. This confirms the assumed linear relation between the muon flux and the coincidence rate (Eq. 3).

7 Conclusions

Data from the first three detection units of the KM3NeT ARCA and ORCA detectors have been used to measure the depth dependence of the atmospheric muon rate. The coincidence rate of multiplicity ≥ 8 is used to select a high-purity sample of atmospheric muons on a DOM-by-DEM basis. With this measurement, the calibration procedure based on coincidence hits from ^{40}K decays is verified. The estimated photon detection efficiencies and time offsets of the PMTs of the KM3NeT detectors are shown to be stable over time. The dependence of the coincidence rate on the depth is found to be compatible with the Bugaev atmospheric muon flux model.

The calibration procedure reported is mature and reliable. Independent of the physical site and depth of the detector, the physics results of KM3NeT ORCA1 and ARCA2 verify the atmospheric muon rate over a range of more than one kilometre. The construction of the ORCA and ARCA detectors by the KM3NeT Collaboration is in progress.

8 Acknowledgements

The authors acknowledge the financial support of the funding agencies: Agence Nationale de la Recherche (contract ANR-15-CE31-0020), Centre National de la Recherche Scientifique (CNRS), Commission Européenne (FEDER fund and Marie Curie Program), Institut Universitaire de France (IUF), IdEx program and UnivEarthS Labex program at Sorbonne Paris Cité (ANR-10-LABX-0023 and ANR-11-IDEX-0005-02), Paris Île-de-France Region, France; Shota Rustaveli National Science Foundation of Georgia (SRNSFG, FR-18-1268), Georgia; Deutsche Forschungsgemeinschaft (DFG), Germany; The General Secretariat of Research and Technology (GSRT), Greece; Istituto Nazionale di Fisica Nucleare (INFN), Ministero dell’Istruzione, dell’Università e della Ricerca (MIUR), PRIN 2017 program (Grant NAT-NET 2017W4HA7S) Italy; Ministry of Higher Education, Scientific Research and Professional Training, Morocco; Nederlandse organisatie voor Wetenschappelijk Onderzoek (NWO), the Netherlands; The National Science Centre, Poland (2015/18/E/ST2/00758); National Authority for Scientific Research (ANCS), Romania; Plan Estatal de Investigación (refs. FPA2015-65150-C3-1-P, -2-P and -3-P, (MINECO/FEDER)), Severo Ochoa Centre of Excellence program (MINECO), Red Consolider MultiDark, (ref. FPA2017-90566-REDC, MINECO) and Prometeo and Grisolia programs (Generalitat Valenciana), “la Caixa” Foundation (ID 100010434) through the fellowship LCF/BQ/IN17/11620019, and the European Union’s Horizon 2020 research and innovation programme under the Marie Skłodowska-Curie grant agreement no. 713673, Spain.

References

1. S. Adrián-Martínez et al. (KM3NeT Collaboration), *Letter of intent for KM3NeT 2.0*, J. Phys. G: Nucl. Part. Phys. **43** (2016) 084001.
2. S. Aiello et al. (KM3NeT Collaboration), *Sensitivity of the KM3NeT/ARCA neutrino telescope to point-like neutrino sources*, Astropart. Phys. **111** (2019) 100–110.
3. S. Adrián-Martínez et al. (KM3NeT Collaboration), *Intrinsic limits on resolutions in muon- and electron-neutrino charged-current events in the KM3NeT/ORCA detector*, JHEP **05** (2017) 008.
4. S. Adrián-Martínez et al. (KM3NeT Collaboration), *Expansion cone for the 3-inch PMTs of the KM3NeT Optical Modules*, JINST **8** (2013) T03006.
5. R. Bruijn, D. van Eijk et al. (for the KM3NeT Collaboration), *The KM3NeT Multi-PMT Digital Optical Module*, PoS(ICRC2015)1157 (2015).
6. S. Adrián-Martínez et al. (KM3NeT Collaboration), *Deep sea tests of a prototype of the KM3NeT digital optical module*, Eur. Phys. J. C **74** (2014) 3056.
7. S. Biagi and A. Orzelli (for the KM3NeT Collaboration), *The Central Logic Board and its auxiliary boards for the optical module of the KM3NeT detector*, JINST **9** (2014) C12033.
8. J.A. Aguilar et al. (ANTARES Collaboration), *Performance of the front-end electronics of the ANTARES neutrino telescope*, Nucl. Instr. Meth. **A622** (2010) 59–73.
9. S. Biagi et al. (for the KM3NeT Collaboration), *The data acquisition system of the KM3NeT detector*, PoS(ICRC2015)1172 (2015).
10. E. de Wolf et al. (for the KM3NeT Collaboration), *A launching vehicle for optical modules of a deep-sea neutrino telescope*, Nucl. Instr. Meth. **A725** (2013) 241.
11. K.W. Melis (for the KM3NeT Collaboration), *In-Situ Calibration of KM3NeT*, PoS(ICRC2017)1059 (2017).
12. M. Colomer, D. Dornic, and V. Kulikovskiy (for the KM3NeT Collaboration), *Detailed KM3NeT optical module simulation with Geant4 and supernova neutrino detection study*, PoS(ICRC2017)983 (2017).
13. Y. Becherini et al., *A parameterisation of single and multiple muons in the deep water or ice*, Astropart. Phys. **25** (2006) 1.
14. A. Margiotta (for the ANTARES Collaboration), *Common simulation tools for large volume neutrino detectors*, Nucl. Instrum. Meth. **A725** (2013) 98.
15. R. Brun et al., *GEANT 3: user’s guide Geant 3.10, Geant 3.11*, <https://cds.cern.ch/record/1119728> (1987) CERN.
16. S. Aiello et al. (KM3NeT Collaboration), *Characterisation of the Hamamatsu photomultipliers for the KM3NeT Neutrino Telescope*, JINST **13** (2018) P05035.

-
17. S. Adrián-Martínez et al. (KM3NeT Collaboration), *The prototype detection unit of the KM3NeT detector*, Eur. Phys. J. C **76** (2016) 54.
 18. A. Albert et al. (ANTARES Collaboration), *Long-term monitoring of the ANTARES optical module efficiencies using ^{40}K decays in sea water*, Eur. Phys. J. C **669** (2018) 78.
 19. G. Riccobene et al., *Deep seawater inherent optical properties in the Southern Ionian Sea*, Astropart. Phys. **27** (2007) 1–9.
 20. E.V. Bugaev et al., *Atmospheric muon flux at sea level, underground, and underwater*, Phys. Rev. D **58** (1998) 054001.
 21. S. I. Klimushin, E. V. Bugaev, and I. A. Sokalski, *On the parametrization of atmospheric muon angular flux underwater*, Phys. Rev. D **64** (2001) 014016.